

1

3 **The application of MEMS seismometers to
4 subregional-scale passive seismology: a case study of
5 the Sercel WiNG nodes.**

6 **Tobermory Mackay-Champion**  *¹, **Thomas Hudson**², **Nicholas Harmon**³, **Christopher Ogden**⁴, **Steve Wilcox**⁵, **Lucy**
7 **Finch**⁶, **Victoria Lane**⁶, **John-Michael Kendall**¹, **Michael C. Daly**¹

8 ¹Department of Earth Sciences, University of Oxford, South Parks Road, Oxford, UK, ²Institute of Geophysics, ETH Zürich, Switzerland,

9 ³Geology and Geophysics, Woods Hole Oceanographic Institution, Woods Hole, Massachusetts 02543, USA, Woods Hole Oceanographic

10 Institute, USA, ⁴School of Geography, Geology and the Environment, University of Leicester, Leicester, UK, ⁵retired from Sercel, ⁶SEIS-UK,
11 University of Leicester, Leicester, UK

12 **Author contributions:** *Conception or design of the study:* Tobermory Mackay-Champion, Thomas Hudson, John-Michael Kendall, Michael C. Daly.

13 *Acquisition, curation, analysis, or interpretation of data:* Tobermory Mackay-Champion, Thomas Hudson, Nicholas Harmon, Chris Ogden, Steve Wilcox, Lucy
14 Finch, Victoria Lane, John-Michael Kendall, Michael C. Daly. *Design and validation of methods and result:* Tobermory Mackay-Champion, Thomas Hudson,
15 Nicholas Harmon, Chris Ogden.

16 **Abstract** Micro ElectroMechanical Systems (MEMS) accelerometers have become increasingly
17 common in geophysical studies. Despite this, no work has been done to assess the suitability of
18 an array of MEMS sensors to low-frequency, regional-scale passive seismic studies. Consequently,
19 a month's-long deployment of twenty MEMS-based Sercel WING nodes, two Guralp CMG-ESPCDS
20 and one 4.5 Hz geophone-Reftek system was undertaken to assess the performance of MEMS ac-
21 celerometers in comparison to conventional seismometers. We show that the WiNG nodes reliably
22 record over 100 Hz to 0.03 Hz, with a -136 dB broadband noise-floor between 100–1 Hz, and a 1/f
23 noise-floor at frequencies below 1 Hz. The nodes accurately recorded earthquakes with epicentral
24 distances ranging from 72° to 40 km. In particular, the low-period (c. 10–30s) surface waves of two
25 teleseismic earthquakes were clearly resolved above the WiNG node's noise floor. A set of three
26 WiNG nodes deployed in a 3-component configuration provided an estimate of the crustal thick-
27 ness beneath Oxford of 39.0 ± 2.0 km using the H-k stacking technique. This compares favourably
28 with the estimate provided by the conventional 3-component ESPCD (37.9 ± 1.3 km) and aligns well
29 with previous results in the literature. The MEMS-based systems have a number of clear advantages
30 over conventional systems, including the speed of deployment, the low cost, the compact design,
31 and the use of an internal battery and GPS. The strong performance of the WiNG nodes during this
32 study shows that these MEMS-based accelerometers are well-suited for passive seismology at a
33 local, regional, and potentially larger scale.

*Corresponding author: tmackaychampion@gmail.com

34 1 Introduction

35 Since the early 2000s, Micro ElectroMechanical Systems (MEMS) accelerometers have become increasingly common
 36 in geophysical studies, particularly within the field of seismic exploration for hydrocarbons (e.g., Laine & Mougenot,
 37 2007). Conventional seismometers, such as geophones, rely on a force-feedback system in which an internal mass
 38 moves in response to ground motion. This movement induces a voltage which is proportional to the ground motion.
 39 Closed-loop MEMS sensors, as opposed to open-loop which demonstrate poorer bandwidth, rely on force-balance
 40 systems which work by recording the voltage required to keep a positive electrode stationary between a pair of
 41 negative electrodes (Herrmann et al., 2021 Liu et al., 2022;). These sensors record in units of acceleration, which
 42 can be readily equated to force. MEMS sensors have a number of advantages over conventional instruments: their
 43 lightweight and compact design makes deploying large arrays easier, the instrument sensitivity to external factors
 44 such as temperature are an order of magnitude less than standard geophones (Laine & Mougenot, 2014), the sen-
 45 sors lack the data jitter seen in geophones (Herrmann et al., 2021), and the instrument response in acceleration is
 46 constant across the frequency domain (Tellier et al., 2020). MEMS sensors have been widely used in a number of
 47 different fields, from regional-local earthquake detection (e.g., d'Alessandro et al., 2014) and the monitoring of local
 48 seismic risk using dense arrays (e.g., Fulawka et al., 2022), to Martian seismology on the NASA InSight Mission (Pike
 49 et al., 2014; e.g., Lognonne et al., 2020) and ocean-bottom deployments (Tellier & Herrmann, 2020). Despite this bur-
 50 geoning utilisation and the proven ability of MEMS sensors to record well below 1 Hz (e.g., Fougerat et al., 2018), no
 51 work has yet assessed the suitability of an array of MEMS sensors for regional-scale passive seismic studies relying on
 52 frequencies below 10 Hz. Given the advantages listed above, MEMS sensors could pose a significant benefit to passive
 53 seismic studies if shown to have the appropriate bandwidth, noise floor and sensitivity. Consequently, we test the
 54 suitability of MEMS-based nodal seismometers to regional passive seismology by comparing the results of an array of
 55 vertical-component Sercel WiNG nodes deployed in Oxfordshire, UK, to the results for two Guralp CMG-ESPCDs and
 56 a 4.5 Hz geophone (connected to a Reftek-RT130 datalogger) which were deployed coincident to the nodes. We focus
 57 on the noise characteristics of the MEMS sensors and the suitability of the array for ambient noise tomography, as
 58 well as the recovery of earthquakes and their application to crustal thickness estimates using H-k stacking of receiver
 59 functions. The Sercel WiNG nodes, deployed in partnership with Sercel and equipped with the latest Sercel MEMS
 60 technology called Quietseis, demonstrate all the requirements of a MEMS seismometer outlined by d'Alessandro et
 61 al. (2019). We therefore view them as a representative case study for the performance of MEMS-based sensors.

62 2 Methods

63 2.1 Array details

64 An array of 20 Sercel WiNG nodes were deployed throughout Oxfordshire between 19th October - 16th November
 65 2020. The array was approximately 50 km long, and trended NW-SE (Fig. 1). At two sites, the WiNG nodes were
 66 deployed alongside more conventional seismometers. The first site, in central Oxford, hosted a 60s-100 Hz Guralp
 67 CMG-ESPCD and a GS-11D 4.5Hz geophone with a RefTek DAS130-01 broadband data logger, and three WiNG nodes
 68 deployed in a 3-component configuration. The second site in north Oxfordshire hosted a 60s-50 Hz Guralp CMG-
 69 ESPCD and a single, vertical-component WiNG node. Both ESPCDs were directly buried, in vaults ~1 m deep. The

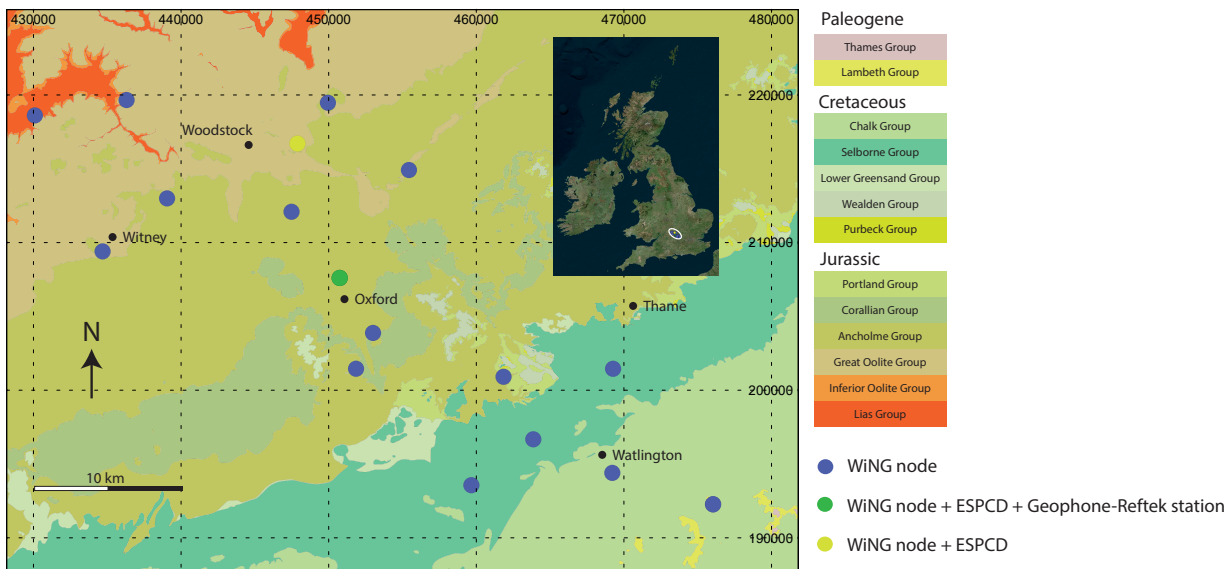


Figure 1 Deployment map. The BGS 1:50K EW236 Whitney Bedrock map is reproduced with the permission of the British Geological Survey © UKRI 2023. All Rights Reserved.

pits were backfilled with soil and sand. The geophone was also buried to a depth of ~30 cm. The WiNG nodes were lightly buried such that the top of the casing was a maximum of 5 cm below the surface. Unlike the geophone and the ESPCD, the WiNG nodes have an internal GPS system. Consequently, the nodes need a shallow burial to prevent loss of the GPS signal. Alternatively, the nodes can be spiked into the ground (Fig. 2).

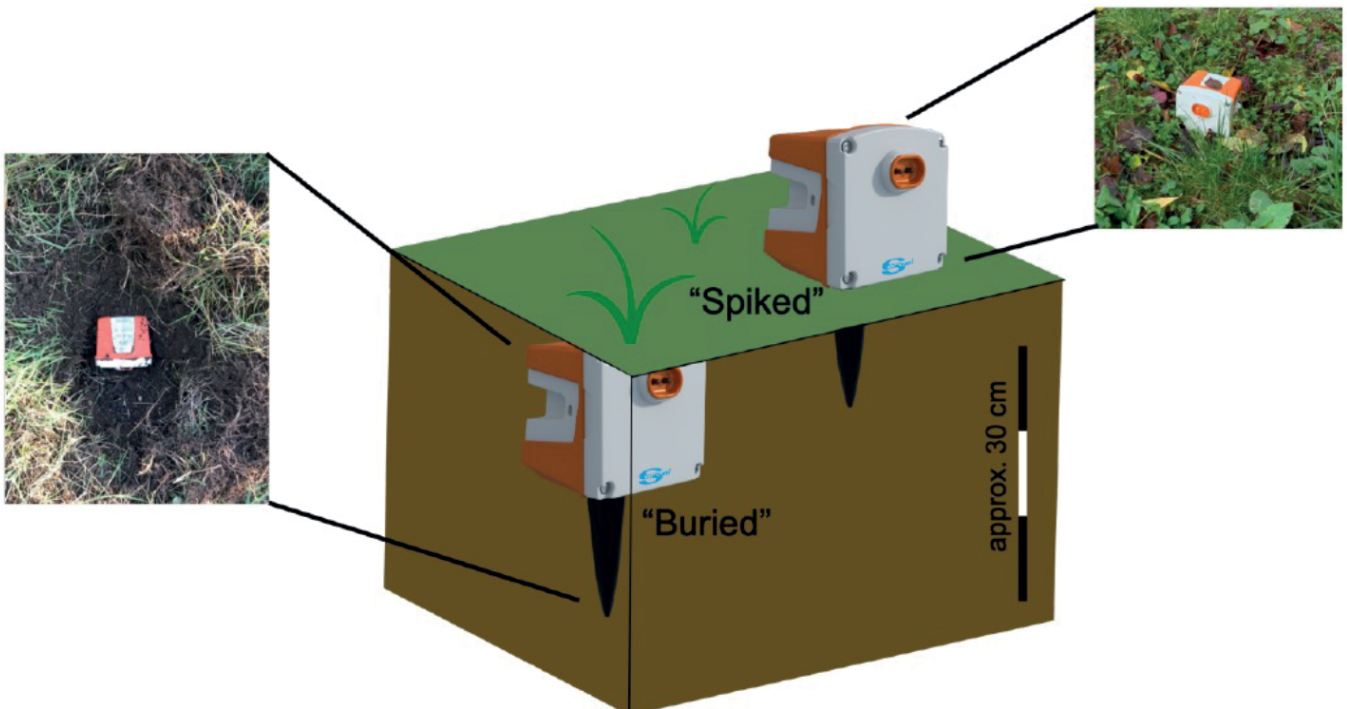


Figure 2 Deployment techniques for the WiNG nodes.

74 2.2 Instrument specifications and response

75 The Sercel WiNG nodes are vertical-component only and use a closed-loop MEMS accelerometer to record ground
 76 motion with an adjustable sampling frequency from 250 to 1000 Hz. They are approximately 750g and are fully self-
 77 contained with their own internal GPS and lithium-ion battery. The battery lasts between 30–50 days, depending on
 78 the instrument set-up. According to the manufacturers, the MEMS sensor has a constant amplitude response across
 79 the frequency domain, with a bandwidth of 0 (DC) to 400 Hz. The noise floor is purported to be $15 \mu\text{ms}^{-2}/\sqrt{\text{Hz}}$
 80 with a constant clip level of 5 ms^{-2} , resulting in a frequency-independent dynamic range of 128 dB. The incoming
 81 acceleration signal is recorded as a 24 bit output, ranging from 2^{-23} to 2^{23} . To be converted back into acceleration,
 82 this bit-value must first be converted into voltage using a scalar value unique to the array (in this case, $67 \mu\text{V/count}$).
 83 The voltage can then be converted into acceleration using the instrument's sensitivity value of 0.425 V/ms^{-2} . This
 84 sensitivity correction is independent of frequency. The manufacturer states a phase accuracy of $< 20 \mu\text{s}$, which is
 85 equivalent to a frequency of 50 kHz. As such, no phase correction is required for the frequency range of interest (Fig.
 86 3A).

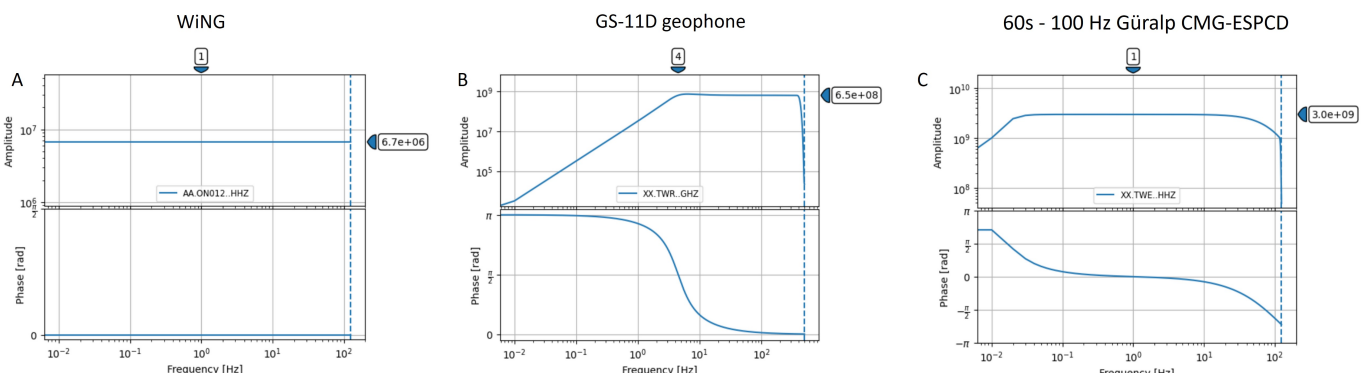


Figure 3 Instrument response Bode plot showing the frequency response of three seismometers from 10^{-2} to 10^2 Hz . A) Sercel WiNG node. B) GS-11D 4.5Hz geophone and RefTek DAS130-01 broadBand data logger. C) 60s-100 Hz Guralp CMG-ESPCD.

87 Two different broadband seismometers were used in the deployment: a 60s-50 Hz Guralp CMG-ESPCD and a
 88 60s-100 Hz Guralp CMG-ESPCD. These instruments are conventional broadband seismometers, measuring ground
 89 velocity, which have been extensively used for passive seismology. They rely on a system of internal masses coupled
 90 with an external battery and GPS unit. These instruments have a flat response in velocity relative to frequency and a
 91 noise-floor below the New Low Noise Model (NLNM) of Peterson (1993) over the given bandwidths. The ESPCD has a
 92 sensitivity of 6000 V/ms^{-1} within the bandwidth, a clip level of 20 V (equivalent to 3.3 mms^{-1}), and a dynamic range
 93 of 165 dB at 1 Hz. Although the clip-level is lower than the WiNG node, the ESPCDs have a lower noise-floor and are
 94 therefore able to attain a larger dynamic range. Like the WiNG node, the ESPCD uses a 24-bit digitizer. This digitizer
 95 has a nominal sensitivity of $1 \mu\text{V/count}$, meaning that the total amplitude correction from counts to velocity is 3×10^9
 96 over the instrument's bandwidth. A phase correction is also required (Fig 3C) across the frequency range.

97 Finally, one GS-11D 4.5Hz geophone was deployed with a RefTek DAS130-01 broadband data logger. This is a force-
 98 feedback system, with a constant frequency response above 4.5 ± 0.75 Hz. Geophones are conventionally used for
 99 monitoring frequencies above their resonant frequency and below a specific spurious frequency (Faber & Maxwell,

1997), however methods such as the cross-correlation of ambient noise data has been successfully applied on geophone data to yield lower frequency information (e.g., Wang et al., 2019). Below the resonant frequency, the sensitivity decays proportional to a damping factor (Havskov & Alguacil, 2016). Above its resonant frequency, the GS-11D geophone has an open-circuit sensitivity of 32 V/ms^{-1} and an open-circuit damping of 34 %. The clip-level and noise floor data are not specified by the manufacturer. Like the ESPCDs, a frequency-dependent phase correction is required for the velocity data (Fig 3B).

2.3 Noise analysis and ambient noise tomography

To ascertain the potential applications of an instrument, it is crucial to understand the performance of said instrument over the frequency range of interest. For microseismic detection, frequencies between 1–50 Hz would be standard whereas regional to sub-regional scale surface wave analysis would require frequencies below 1 Hz. As such, the MEMS sensors need to demonstrate a wide bandwidth if they are to be of use in passive seismology. To examine this, probabilistic power spectral densities were constructed for the co-located WiNG node, ESPCD and geophone following the methodology of McNamara & Buland (2004). First, the instrument response was removed and the ESPCD and geophone data were differentiated into acceleration. The data were then downsampled to 250 Hz, representing a factor of four for the geophone, a factor of two for the MEMS sensor and no downsampling for the ESPCD. Then the time window of interest (in this case, 1 day) was split into sliding windows of 60mins, with a 50 % overlap between windows. The Power Spectral Density, PSD, $((\text{m/s}^2)^2/\text{Hz})$ was calculated using the Welch Method for each window, and then converted into decibels relative to $1(\text{m/s}^2)^2/\text{Hz}$ (Welch, 1967). These are the units used by the noise models of Peterson (1993). The PSDs were then downsampled into 1/8th octave bins, and the probability at each frequency point was calculated following Equation 4 of McNamara & Buland (2004).

Ambient Noise Tomography (ANT), and array beamforming of the cross correlations, were used to examine the frequency range of surface waves recorded by the array of WiNG nodes and to assess the suitability of the array to ambient surface wave tomography. ANT uses the phase information of cross-correlations between the ambient recordings of pairs of stations to examine the seismic velocity structure within an array. Prior to the calculation of the cross-correlations, a 1-bit amplitude normalisation, downsampling to 4 Hz and a moving-average frequency normalisation (“spectral whitening”) was performed to the raw seismograms, following Bensen et al. (2007). The seismograms for each instrument were binned into 4hr-long sections, and the cross-correlation for each station-pair was calculated for each bin. A linear stack was then taken of every bin for each individual cross-correlation to create a final cross-correlation for each station pair (420 total). Only the WiNG nodes were included in the analysis, as it was important to determine their performance alone. Following stacking, array-scale beamforming (following Gerstoft et al., 2006) was performed to determine the phase velocity of waves travelling through the entire array. The average phase velocity for the array provided by this step is useful for resolving the cycle ambiguity when determining the dispersion for individual station-pair cross correlations. The phase dispersion for each pair of stations was then estimated by unwrapping the phase of the Fourier transformed cross-correlations, using the average phase velocity calculated in the array beamforming to provide an initial estimate of the total number of wavelengths between each pair of stations for a given period. The observed phase from all useable station pairs at each period of interested was then inverted for 2-D surface-wave phase velocity maps across the region using a damped, weighted least-squares

following Harmon & Rychert (2016). The inversion uses a nodal parameterization, where the phase velocity at each point in the map is a weighted average of the nearby nodes. We use the average phase velocity at each period from the beamforming as our uniform starting velocity. A damping parameter of 0.2km/s was chosen based on previous work (Harmon & Rychert 2016), with a constant weighting throughout the model.

A pseudo-dispersion curve was created for a representative point within the middle of the array using the phase velocity for that point from the 2-D phase velocity maps for each period of interest. This curve was then inverted for S-wave velocity with depth using an iterative non-linear inversion (Rychert & Harmon, 2016; Tarantola & Valette, 1982). The inversion starting model consisted of 30 layers, each 1 km thick, with an initial velocity of 4.2 km/s for each layer, following Hermann (2013). A chi-squared objective function was used, with a value of < 1 being indicative of good fit.

2.4 Earthquake analysis

The analysis of earthquakes, on a regional and local scale, is fundamental to many techniques in seismology. MEMS sensors must reliably detect and record these earthquakes if they are to be of wide use. Teleseismic earthquakes are of particular interest, because the sensor would need to have a low enough noise floor to suitably detect highly attenuated, low frequency waves. As such, the performance of the MEMS sensors was examined for two teleseismic earthquakes and several local to regional earthquakes.

2.4.1 Receiver Functions

Arrivals from teleseismic earthquakes can be used to examine the crustal structure beneath a seismometer. One such method is known as H-k stacking (Zhu & Kanamori, 2000), which uses Receiver Functions (RF) to provide an estimate of crustal thickness (H) and the bulk crustal Vp/Vs ratio (k), following Equation 1.

$$s(H, k) = \sum_{j=1}^N w_1 r_j(t_1) + w_2 r_j(t_2) - w_3 r_j(t_3) \quad (1)$$

Where N is the number of receiver functions, w_1 , w_2 , w_3 are stacking weightings, t_1 , t_2 , t_3 are the travel times of the Ps , $PpPs$ and $PsPs+PpSs$ phase respectively, and $r_j(t_i)$ are the amplitudes of the respective phases. We calculated RFs using the time-domain iterative deconvolution method of Ligorria & Ammon (1999), with Gaussian width factors of between 0.8–4.0. Following the modified H-k stacking approach of Ogden et al. (2019), which overcomes some of the parameter sensitivity issues discussed therein, we computed 1,000 individual H-k results using the calculated RFs and randomly selected input parameters for each station of interest. Cluster analysis is then used to determine the best-fitting result as well as the reliability of the result for that station. RF analysis requires 3-component systems as it involves the deconvolution of the radial component from the vertical component seismograms. Consequently, we are unable to perform RF analysis on a single node because the WiNG nodes record vertical-component information only. However, the MEMS electronics is not sensitive to the component direction. As such, 3 separate WiNG nodes were deployed in a 3-component configuration and the RF analysis was performed on this combined system. The results were then compared to the results obtained from the conventional 3-component ESPCD deployed at the same site.

171 3 Results

172 3.1 Ambient noise analysis

173 The Probabilistic Power Spectral Densities (PPSD) illuminate several key differences between the co-deployed 60s–100 Hz ESPCD, 4.5 Hz geophone, and the WiNG node (MEMS sensor) (Fig. 4). This site was located in central Oxford,

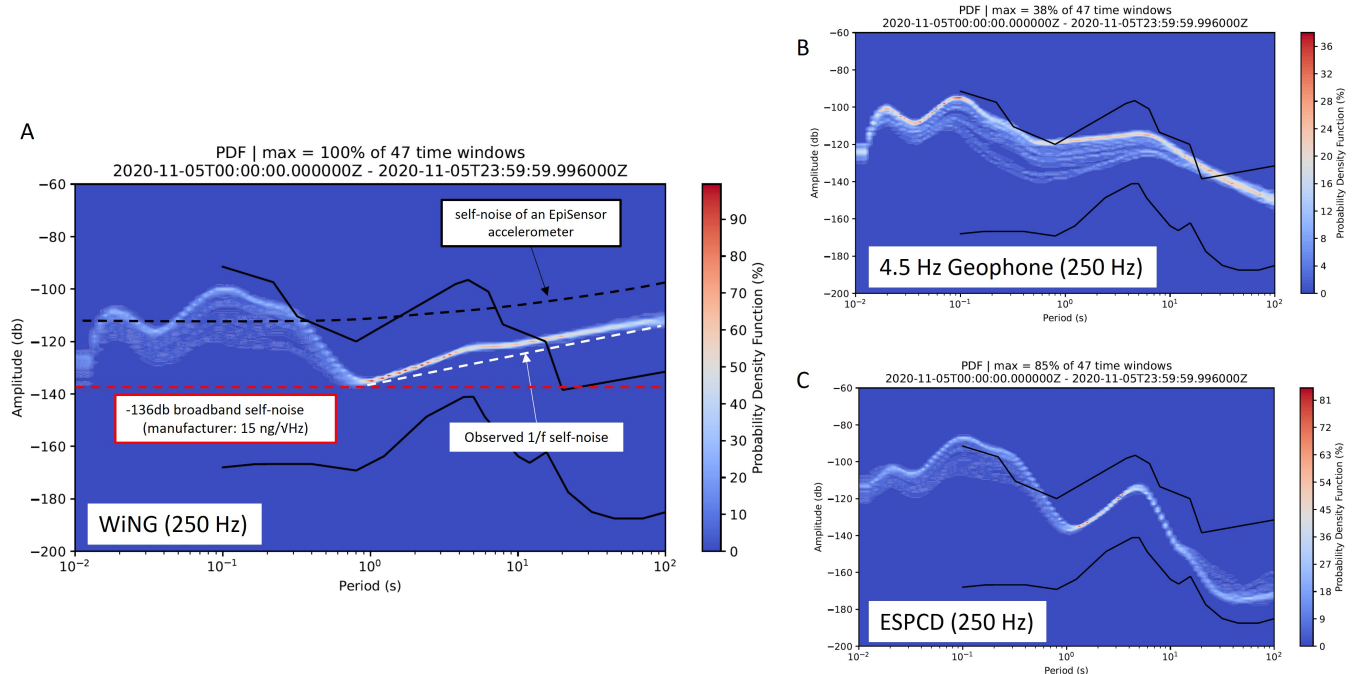


Figure 4 Probabilistic Power Spectral Density analysis for 5th November 2020. A) Sercel WiNG node. B) 4.5 Hz Geophone. C) 60s–100 Hz ESPCD. Each instrument has a sampling frequency of 250 Hz in units of acceleration for this analysis. The solid black lines are the New High Noise Model (top) and New Low Noise Model (bottom) of Peterson (1993).

174 and consequently has a high level of anthropogenic noise between 100–10 Hz. All of the three instruments show a
 175 similar topology between 100–10 Hz, with amplitudes of between -130 to -85 dB and clear peaks at approximately 90
 176 Hz and 10 Hz. The geophone and ESPCD both show higher amplitudes throughout this frequency range compared to
 177 the WiNG node, which may be due to being closer to the source of the noise or more likely to do with a higher degree
 178 of coupling with the ground. The WiNG node was buried in topsoil, which may have contributed a degree of damping
 179 of the high frequency signals, while the geophone was buried more deeply (~30 cm), and the ESPCD was buried even
 180 more deeply (~1 m). All three instruments see a reduction in amplitude for signals between 10 to 1 Hz. The ESPCD
 181 shows an amplitude reduction of ~70 dB and the WiNG node shows a reduction of ~60 dB. The geophone displays
 182 a smaller change of only ~25 dB, likely due to the geophone's resonance at 4.5 Hz. Nevertheless, the reduction in
 183 amplitude seen by each instrument corresponds well with the reduction seen in the New High Noise Model (NHNM)
 184 of Peterson (1993). The MEMS sensor and the ESPCD both show a tightly clustered amplitude of approximately -135
 185 to -140 dB, with an amplitude trough at 1 Hz. On the other hand, the geophone displays a trough at ~4 Hz, and exhibits
 186 a significant spread in amplitude from -140 dB up to -120 dB. This larger spread in amplitude no doubt corresponds
 187 to the change in behaviour of the geophone at its resonant frequency.

188 At periods larger than 1 s, the behaviour of the three instruments diverges. Below 1 s, the WiNG node displays a
 189 broadband noise floor of $15 \mu\text{ms}^{-2}/\sqrt{\text{Hz}}$, equivalent to a constant noise of -136 dB. Signals with amplitudes below
 190 this noise floor would not be distinguishable from the background random noise of the sensor. This is some way

above the New Low Noise Model (NLNM) of Peterson (1993), suggesting that the sensors would not perform well in seismically quiet areas. Above 1 s, the WiNG node shows a tightly clustered amplitude with a slope of $1/f$. This is a well-known feature of electrical circuits known as ‘flicker noise’ or ‘pink noise’ and decreases the dynamic range of the sensor at the affected periods (Sleeman et al., 2006). As with the broadband noise floor, any signal of interest would need to have an amplitude above the $1/f$ noise if it were to be adequately detected. The primary microseism at 5–8 s is an example of such a signal, which can be clearly seen above the noise floor. The noise floor of a widely used force-balance accelerometer known as the EpiSensor is plotted for comparison, after Koymans et al. (2021). The WiNG node displays a lower noise floor, making it more suitable for passive seismology. The geophone also records the primary microseism, although the variation in amplitude of -125 to -115 dB is likely caused by the resonance of the geophone and does not present variations in the primary microseism itself. This is surmised because the ESPCD displays a tight clustering of amplitude at -115 dB for the primary microseism. Beyond the primary microseism, the geophone displays a linear drop in amplitude. This is indicative of a drop in sensitivity and suggests that the low-frequency corner of the bandwidth has been exceeded. As already mentioned, the ESPCD displays a clear primary microseism, and a secondary microseism can also be detected at around 12–15 s. The strength of this secondary microseism clearly varies with the time window. Above 30 s, the ESPCD exhibits a plateau in amplitude indicative of ‘the hum’ (Kobayashi & Nishida, 1998 etc.). The amplitudes observed by the ESPCD fall well within the NHNM to NLNM window at periods above 1 s and are consequently above the stated noise floor of the instrument.

3.2 Ambient noise tomography

The flicker noise displayed by the WiNG nodes below 1Hz is random (Halford, 1986). Consequently, cross-correlations between pairs of stations will be independent of flicker noise when stacked over a sufficient period of time. The cross-correlation of the ambient noise between the 20 station pairs creates a clear moveout of approximately 3 km/s, which is indicative of Rayleigh waves travelling through the array of WiNG nodes (Fig. 5A).

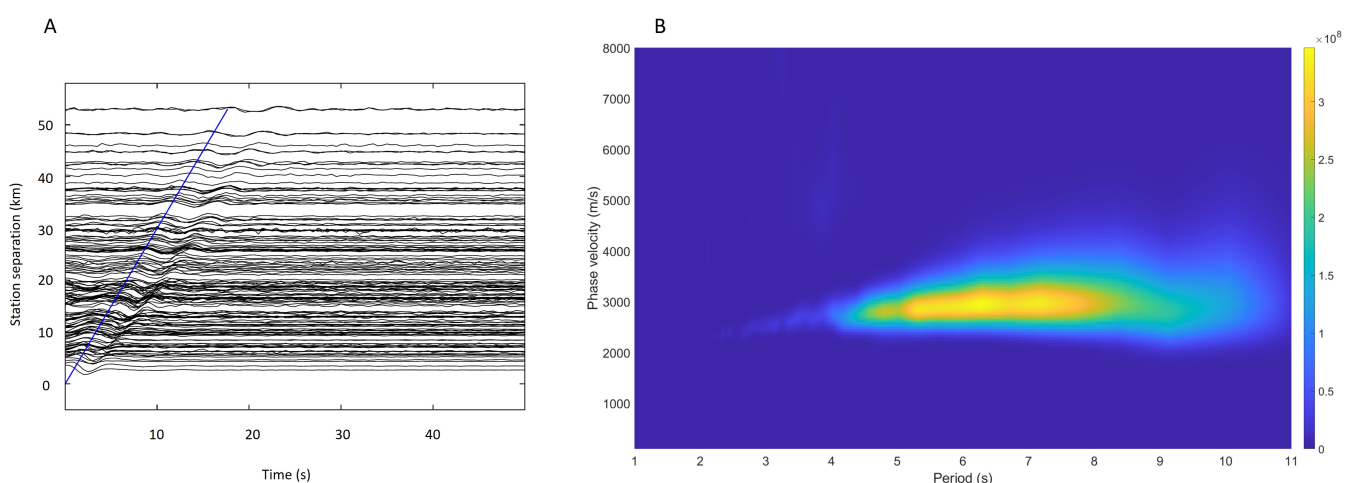


Figure 5 A) One-side cross-correlation moveout. The blue line corresponds to a velocity of 3 km/s. B) Array beamforming surface wave dispersion.

The array beamforming of these cross-correlations demonstrates that the array can detect surface waves with periods of at least 7.5 s (Fig. 5B). The phase velocities are all within an appropriate range of 2.8–3.5 km/s, indicative of crustal Rayleigh Waves (e.g., Harmon & Rychert, 2016). The maximum station separation in the array is approxi-

217 mately 50 km. Given that the phase velocity of a given surface wave can only be accurately determined if the station
 218 separation is equal to at least 2 wavelengths (Harmon et al., 2008), the 7.5 s upper period limit was imposed on the
 219 array by the station separation and not the performance of the sensors themselves. As will be shown in Section 3.3,
 220 the WiNG nodes can reliably record signals below 20 seconds.

221 The 2-D surface-wave phase velocity maps, and associated error maps, constructed for the range of periods found
 222 in the array beamforming demonstrate that the array is detecting lateral velocity contrasts greater than the measure-
 223 ment error (Fig. 6). The phase velocity map for a 3 s surface wave (Fig. 6A) shows many similarities to the geological
 224 map of Fig. 1, suggesting that the detected velocity contrasts are realistic.

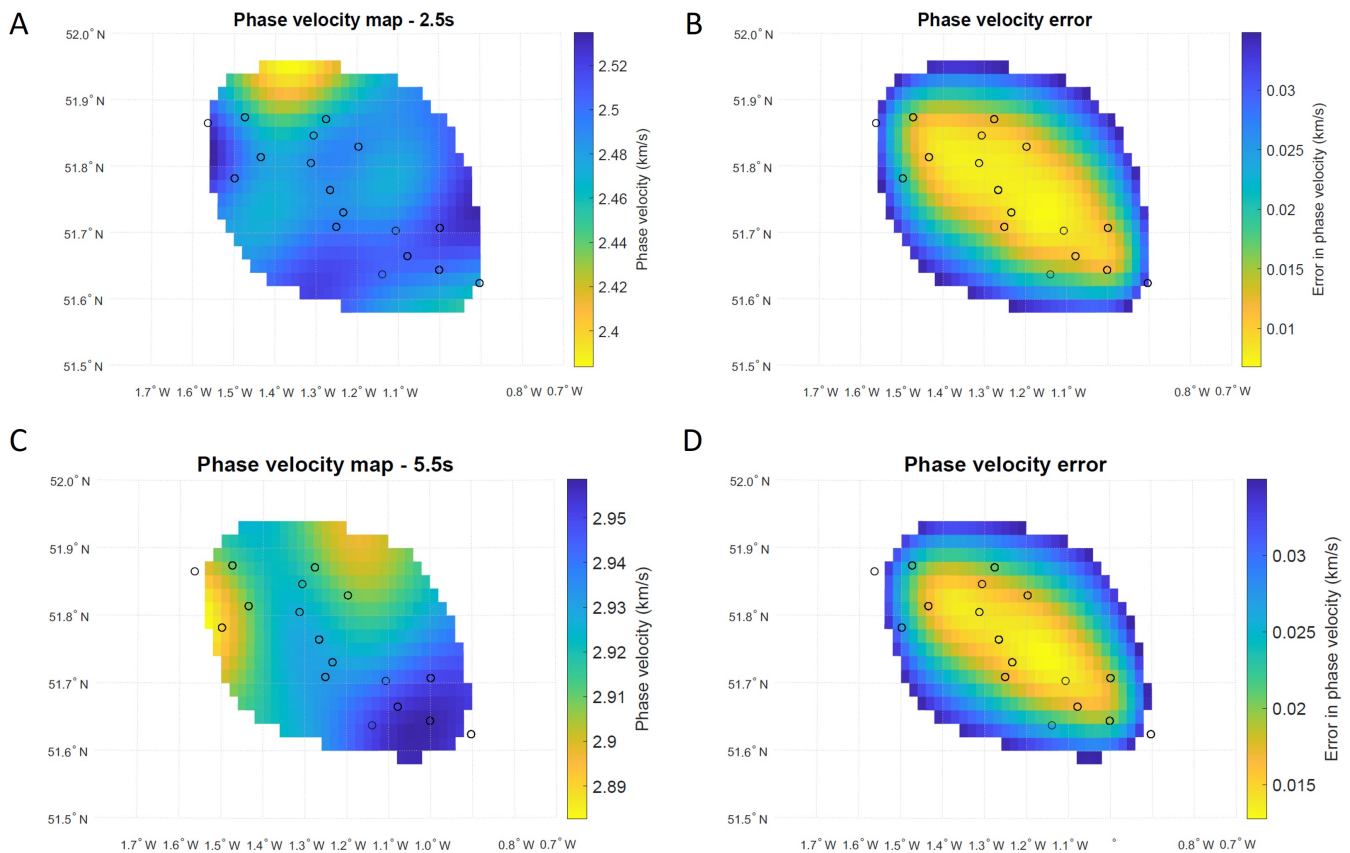


Figure 6 2-D phase velocity maps. A) Phase velocity map of 2.5 s wave. B) Error in the phase velocity measurements at 2.5 s. C) Phase velocity map of 5.5 s wave. D) Error in the phase velocity measurements at 5.5 s. Locations with an error value above 0.04 km/s are masked.

225 A representative surface wave dispersion curve for the middle of the array was constructed using the phase ve-
 226 locity maps for each period of interest and inverted for S-wave velocity against depth (Fig. 7). The sensitivity of the
 227 surface waves for the period range of interest shows a peak sensitivity to depths between 2–10 km, followed by a
 228 steady decline in sensitivity to a maximum depth of 20 km (Fig. 7B). The “best-fit” S-wave solution comprised 4 km
 229 layers with a stepwise increase in S-wave velocity, from a minimum of 2.6 km/s at the surface to a maximum of 3.9
 230 km/s at a depth of 20 km. The large step increase in velocity below 4 km likely represents the sediment–basement
 231 interface, which is thought to be at a depth of approximately 4–5 km (Wright & Cox, 2001; Woodcock & Stachan, 2012).

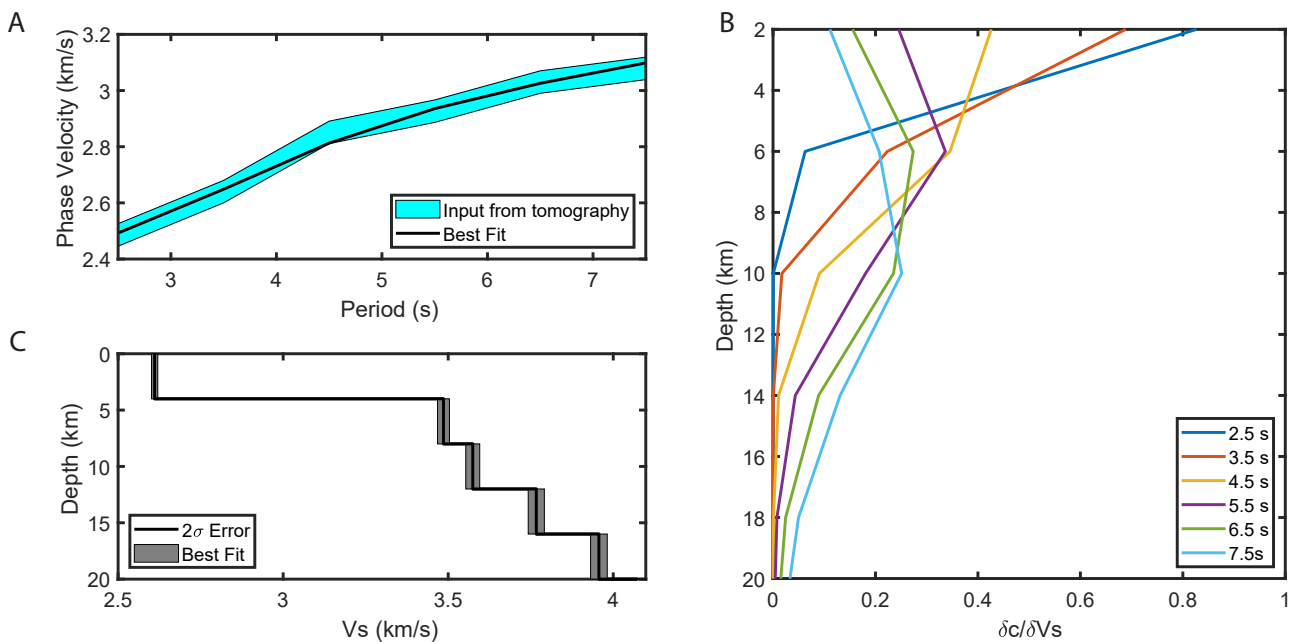


Figure 7 One-dimensional S-wave inversion. A) The observed dispersion curve, and the forward modelled dispersion curve. B) The resulting S-wave velocity profile. C) The depth sensitivity of the surface waves used in the inversion.

3.3 Earthquake analysis

For the MEMS accelerometer to prove useful to the field of passive seismology, it must be able to detect local to teleseismic earthquakes. This provides several tests for the sensor. In particular, the low frequency arrivals associated with teleseismic earthquakes, such as the < 1Hz surface waves, must be above the $1/f$ noise floor if they are to be adequately resolved at individual stations. For more local earthquakes, the high frequency arrivals need to be resolved from the background anthropogenic noise.

A MW 7.6 earthquake from Alaska was recorded by the array on 19th October 2020, from an epicentral distance of 72 °(British Geological Survey, 2020) (Fig. 8). The Power Spectral Density plot shows that both the WiNG node and the ESPCD measure a peak in amplitude at periods 20–30 s, corresponding to the arrival of the low period surface wave (Fig. 8A). This arrival is well above the $1/f$ noise floor of the MEMS sensor so can be clearly resolved. In contrast, the geophone shows a far broader area of increased amplitude. The lower amplitude of the WiNG node peak (-95 dB) in comparison to the peak of the ESPCD (-75 dB) is likely caused by the higher quality of coupling between the ESPCD and the ground provided by the deep burial of the seismometer. With a low-pass filter of 1 Hz, all three instruments show a clear P-wave arrival (Fig. 8B, G, L). The surface wave train is clear in the ESPCD and WiNG record, but largely absent from the geophone data. At a low-pass filter of 10 Hz, the surface waves dominate the signal. The ESPCD and WiNG data are similar, although the WiNG node has a higher noise floor (Fig. 8C, H). The surface wave train is not smoothly recorded by the geophone, although similar arrivals can be identified (Fig. 8M). The dispersion of the surface waves can be clearly observed in the WiNG and ESPCD data. For example, the arrival time of the surface wave train with a 20 Hz low-pass filter (Fig. 8D) is later than the 30 Hz filter (Fig. 8E), which is later than the 40 Hz filter (Fig. 8F). The WiNG node reliably records signals down to 20 Hz (Fig. 8I). At 30 Hz, a surface wave arrival can still be seen (Fig. 8J), although the noise floor is high and some of the signal is clearly lost. No signal is observed below 40

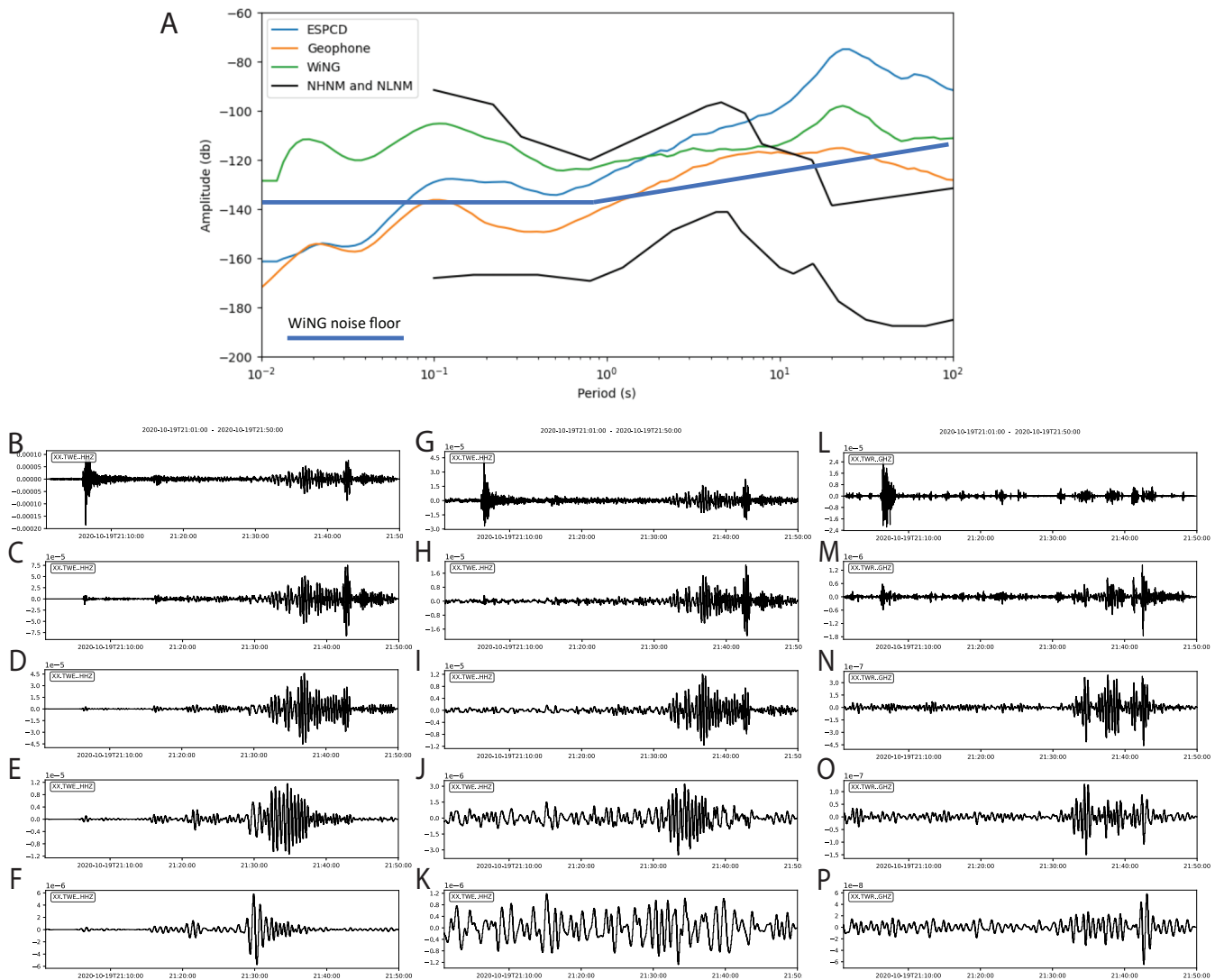


Figure 8 Instrument response to a MW 7.6 Alaska earthquake on 19th Oct. 2020. A) Instrument Power Spectral Density, in units of acceleration decibels relative to 1. (B, C, D, E, F) ESPCD acceleration data with a 1 s, 10 s, 20 s, 30 s and 40 s low-pass filter, respectively. (G, H, I, J, K) WiNG node acceleration data with a 1 s, 10 s, 20 s, 30 s and 40 s low-pass filter, respectively. (L, M, N, O, P) 4.5 Hz geophone acceleration data with a 1 s, 10 s, 20 s, 30 s and 40 s low-pass filter, respectively.

253 Hz (Fig. 8K). Although this performance is notably worse than the broadband ESPCD, these results show that MEMS
254 accelerometers are capable of reliably recording low-frequency arrivals.

255 The strong performance of the WiNG node at low frequencies is repeated for the MW 7.0 earthquake from Greece,
256 which occurred at an epicentral distance of 24°(USGS, 2020). The earthquake can be clearly seen arriving at all of the
257 deployed node stations (Fig. 9). Akin to the Alaska earthquake, a clear P and surface wave arrival can be observed,
258 and the amplitude of the arrivals is demonstrably higher than the sensor noise floor (Fig. 10). The WiNG nodes also
259 perform well in regional and local earthquakes. The MW 2.7 North Sea earthquake (epicentral distance of 6.45 (British
260 Geological Survey, 2020)) shows clear arrivals between 3–6 Hz (Fig. 10A, B), and the low MW 0.9 Worcester earthquake
261 (epicentral distance of 0.64°(British Geological Survey, 2020) can also be distinguished from the background noise
262 (Fig. 10D, E).

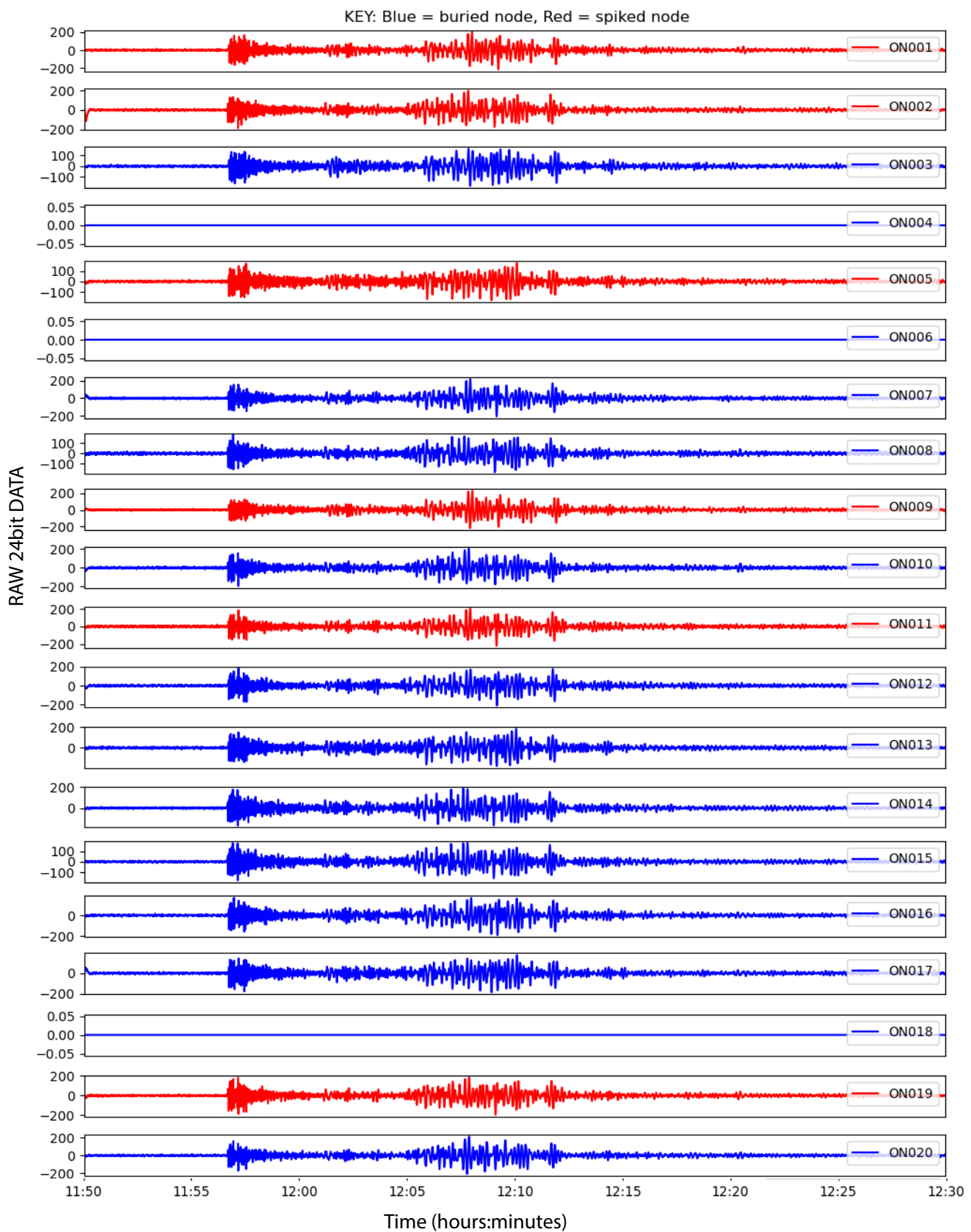


Figure 9 The response of the WiNG node array to the Greece Earthquake (MW 7.0), 30th Oct. 2020. A bandpass filter of 0.05–1 Hz has been applied. The blue plots correspond to nodes that were buried underground. The red plots correspond to nodes that were spiked into the ground (see Fig. 2).

263 3.3.1 Crustal thickness estimate

264 Due to the short deployment time of only 28 days, there were only four earthquakes recorded with an epicentral
 265 distance between 30° - 90° from which to calculate receiver functions, and only one of these earthquakes produced an
 12

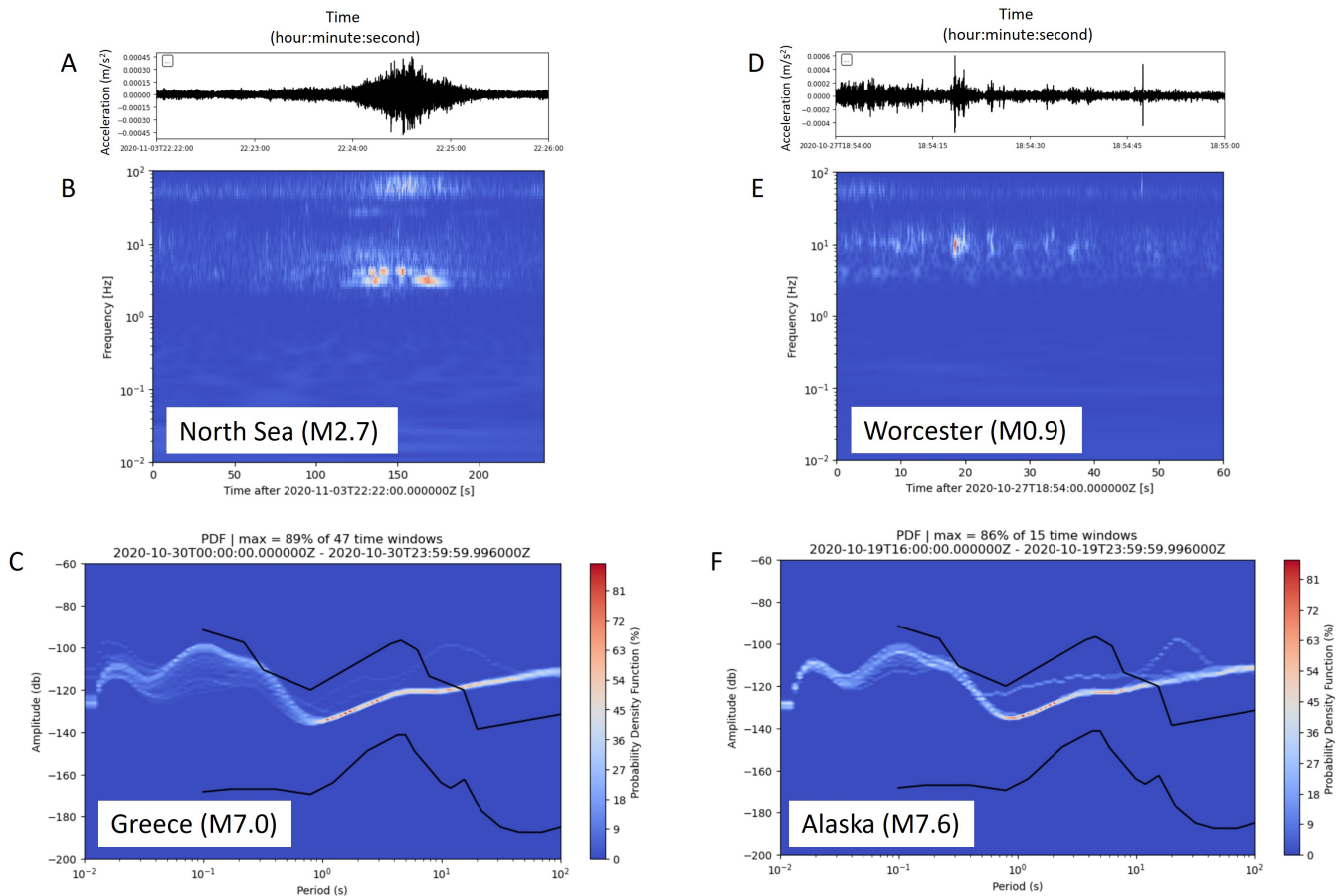


Figure 10 Response of the ON012 WiNG node to a selection of earthquakes. A) WiNG node response to the MW 2.7 North Sea earthquake; B) A continuous-wavelet-transform analysis of the North Sea earthquake. C) PPSD analysis of 30th Oct. 2020, featuring the MW 7.0 Greece earthquake; D) WiNG node response to the MW 0.9 Worcester earthquake; E) A continuous-wavelet-transform analysis of the Worcester earthquake; F) PPSD analysis of 19th Oct. 2020, featuring the MW 7.6 Alaska earthquake.

adequate receiver function (the Alaska earthquake of Fig. 8). Nevertheless, both the ESPCD and the 3C-WiNG system recorded this earthquake and therefore a comparison between the ESPCD-derived RF and the WiNG-derived RF is possible (Fig. 11).

The RFs are shown for both 1.0 Hz and 2.0 Hz, corresponding to a Gaussian width factor of 2.0 and 4.0 respectively. The WiNG-derived RF shows a strong similarity with the ESPCD-derived RF at each frequency, particularly within the 0–10 s range. The ESPCD system provided a crustal thickness estimate of 37.9 ± 1.3 km and a Vp/Vs ratio of 1.78 ± 0.02 (Fig. 12A), while the 3C-WiNG system provided a crustal thickness estimate of 39.0 ± 2.0 km and a Vp/Vs ratio of 1.77 ± 0.04 (Fig. 12B). These two estimates of crustal thickness both agree within error. Although these results are only based on a single earthquake, the values align well with the crustal thicknesses (36–39 km) and Vp/Vs ratios (1.72–1.77) calculated by Tomlinson et al. (2006) for the Midland Microcraton, on which Oxford lies.

4 Discussion

The MEMS sensor has been shown to record accurate information over a wide range of frequencies suitable for passive seismology. The self-noise of an instrument is a fundamental limit on its ability to record events. The WiNG nodes are characterised by a broadband noisefloor of -136dB for periods between 1s to 0.01 s. This is significantly below the NHNM, so signals within this frequency range will likely be recorded reliably. At periods above 1 s, “flicker”

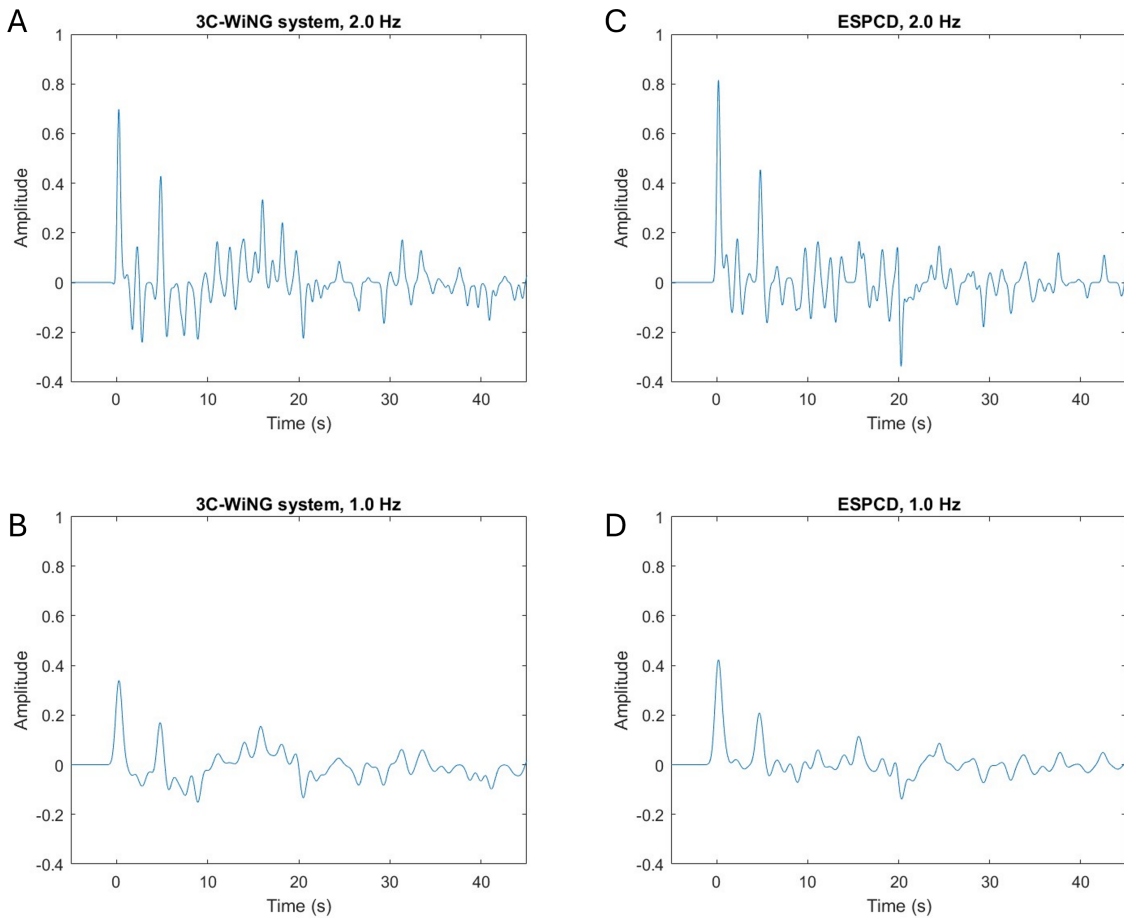


Figure 11 Receiver functions calculated for the MW 7.6 Alaska earthquake on 19th Oct. 2020. A) 2.0 Hz RF for the 3C-WiNG system. B) 1.0 Hz RF for the 3C-WiNG system. C) 2.0 Hz RF for the 60s–100 Hz Güralp ESPCD. D) 1.0 Hz RF for the 60s–100 Hz ESPCD.

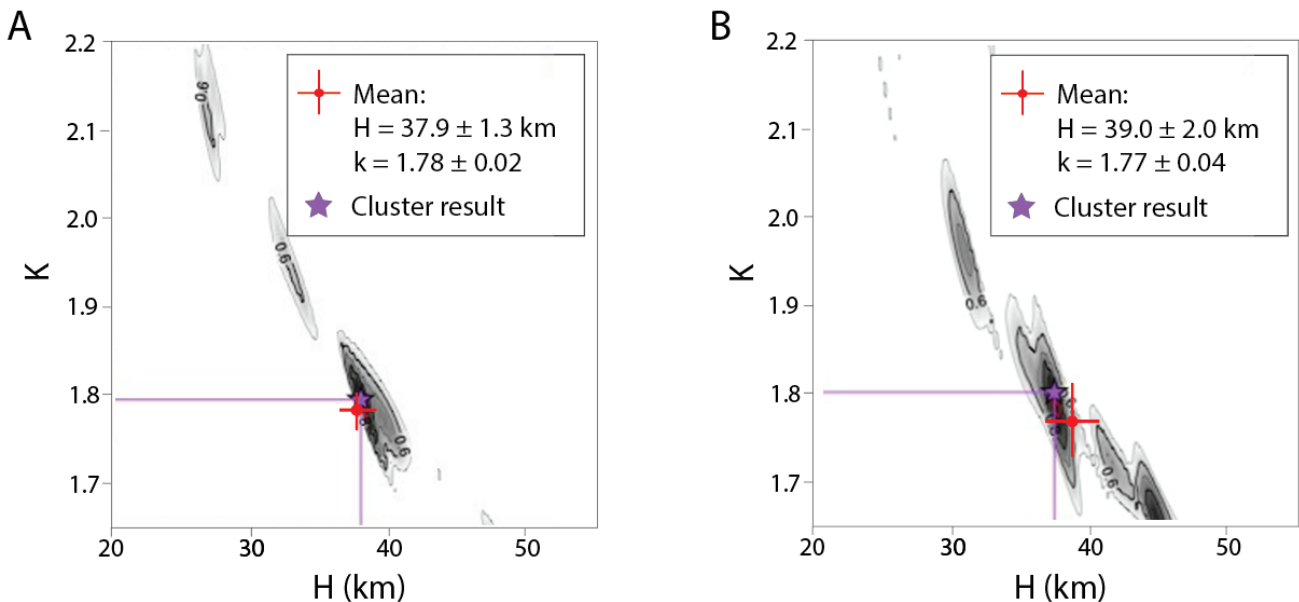


Figure 12 H-k stacking results. A) 60s–100 Hz Güralp ESPCD. B) 3C-WiNG system.

noise with a slope of $1/f$ exceeds the broadband noise-floor and surpasses the NHNM at around 15–20 s period. Consequently, it is possible that arrivals in this frequency range may be masked by the “flicker” noise. However, this study has shown that low-frequency surface waves from teleseismic earthquakes can be well resolved in both the time and frequency domain, with reliable measurement down to 30 s. At periods less than 30 s, the WiNG data compares well with that of the ESPCD (Fig. 8). It should be noted that the WiNG nodes were all deployed in relatively water-rich topsoil, with only centimetre-scale burial, whereas the ESPCDs were directly buried in vaults ~1m deep. As such, the 30 s limit may represent a coupling or damping issue and the low-frequency limit might improve at drier, firmer sites.

The random nature of the flicker noise also meant that cross-correlation techniques proved able to extract meaningful phase information from ambient surface waves travelling across the array, up to a period of at least 7.5 s. Given the low-frequency performance of the WiNG nodes, the 7.5 s limit of the array beamforming is more than likely imposed by the relatively small instrument spacing within the array. It seems probable that the WiNG nodes could be used for regional and country-scale ambient noise and earthquake surface-wave tomography studies if an appropriate instrument spacing is used. The pseudo-3C WiNG system performed well for the receiver function analysis, providing a crustal thickness estimate within error of that achieved by the conventional ESCPD. The WiNG system had a larger error to its estimate, but that can largely be accounted for by the lack of rigid orthogonality and potential tilting of the 3 separate WiNG nodes (doubling as the three separate components) during the deployment. The manufacturer of the WiNG nodes has developed a metal stage to ensure orthogonality and reduce the effects of tilting. Given this, the WiNG nodes are certainly suitable for receiver function analysis.

The WiNG nodes, and other such nodal systems which rely on a MEMS accelerometer, have many clear advantages over the conventional seismometer systems. The nodes are significantly cheaper, costing £100s in comparison to the average ESPCD set-up costing £10,000s. The nodes can be deployed within a matter of minutes, versus a number of hours for the average ESPCD deployment. The nodes leave a far smaller surface footprint once deployed, which greatly helps with site security. The nodes are fully integrated with an internal GPS and lithium-ion battery, so require no supporting equipment, and therefore provide a smaller logistical challenge when deploying a large array. The low cost, smaller size, and high speed of deployment means a large array of instruments can be deployed more easily and in a smaller time frame. However, the integrated nature of the nodal systems presents several disadvantages when compared with conventional seismometers. The internal GPS means that the node cannot be buried to a great depth because this would obscure the signal of the GPS. Geophones and ESPCDs rely on external GPS systems, meaning the seismometers can be buried at any depth and connected to a GPS on the surface. This increased depth of burial improves coupling with the ground, as can be seen by the higher amplitudes of the teleseismic arrivals in the ESPCD data when compared to the WiNG node data. The burial also shields the seismometer from signals of no interest, such as shallow anthropogenic noise. Finally, deep burial does make the seismometer more difficult to recover which can deter would-be thieves. The WiNG nodes also rely on an internal battery, which means that they can only record for a maximum of 50 days. For longer deployments, this means multiple trips into the field for re-charging. A final disadvantage of the MEMS sensor is the flicker noise below 1 Hz, which is an attribute of all electronic circuits. This means that low amplitude signals could be obscured by the noise-floor of the sensor, particularly at low-noise sites

³¹⁸ and especially at periods greater than 15–20 s where the noise surpasses the NHNM.

³¹⁹ 5 Conclusions

³²⁰ This study has shown that the WiNG nodes reliably record over 100 Hz to 0.03 Hz, with a -136 dB broadband noise-
³²¹ floor between 100–1 Hz, and a 1/f noise-floor at frequencies below 1 Hz. The nodes reliably recorded a range of
³²² earthquakes, with epicentral distances from 72° to 40 km. In particular, the low-period (*ca.* 10–30 s) surface waves
³²³ of two teleseismic earthquakes were clearly resolved above the sensor's noise floor. The cross-correlation of pairs
³²⁴ of nodes provided information on ambient surface waves down to a period of at least 7.5 s, which provided sensi-
³²⁵ tivity to seismic velocities down to a depth of 20 km. The 7.5 s limit represents a limit enforced by the maximum
³²⁶ station separations within the array and not the instruments themselves. A set of three WiNG nodes deployed in a
³²⁷ 3-component configuration provided an accurate estimate of the crustal thickness beneath Oxford of 39.0 ± 2.0 km
³²⁸ using the H-k stacking technique of Ogden et al. (2019) on a calculated receiver function from a teleseismic MW 7.0
³²⁹ earthquake in Alaska. This estimate is in error of the estimate provided by the conventional 3-component ESPCD
³³⁰ of 37.9 ± 1.3 km and aligns well with previous results in the literature. The nodal systems have a number of clear
³³¹ advantages over conventional systems, including speed of deployment, cost, small size. These advantages mean a
³³² large array of MEMS sensors could be deployed cheaply, easily and in a short time frame. The disadvantages include
³³³ the restricted depth of burial, which reduces coupling and increases noise levels, and the limited life of the internal
³³⁴ battery system. In conclusion, the strong performance of the WiNG nodes at frequencies above and below 1 Hz, in
³³⁵ both ambient noise and earthquake analysis, shows that MEMS-based nodes are well-suited for passive seismology
³³⁶ studies at a local, regional, and potentially larger scale.

³³⁷ Acknowledgements

³³⁸ We would like to thank Sercel for the donation of the Sercel WiNG nodal seismometers. Michael C. Daly would like
³³⁹ to acknowledge funding from NERC CuBES WP1 Reference No. NE/T003170/1.

³⁴⁰ Data and code availability

³⁴¹ The data and codes for this project are available on Zenodo: 10.5281/zenodo.10909542.

³⁴² Competing interests

³⁴³ The Sercel WiNG nodes were deployed in partnership with Sercel.

³⁴⁴ References

- ³⁴⁵ Bensen, G. D., Ritzwoller, M. H., Barmin, M. P., Levshin, A. L., Lin, F., Moschetti, M. P., Shapiro, N. M., and Yang, Y. Processing seismic ambient
³⁴⁶ noise data to obtain reliable broad-band surface wave dispersion measurements. *Geophysical Journal International*, 169:1239–1260, 6
³⁴⁷ 2007. doi: 10.1111/j.1365-246X.2007.03374.x.
- ³⁴⁸ d'Alessandro, A., Luzio, D., and D'Anna, G. Urban MEMS based seismic network for post-earthquakes rapid disaster assessment. *Advances*
³⁴⁹ *in Geosciences*, 40:1–9, 9 2014. doi: 10.5194/adgeo-40-1-2014.

- 350 d'Alessandro, A., Scudero, S., and Vitale, G. A Review of the Capacitive MEMS for Seismology. *Sensors*, 19:3093, 7 2019.
351 doi: 10.3390/s19143093.
- 352 Ekström, G., Nettles, M., and Dziewoński, A. The global CMT project 2004–2010: Centroid-moment tensors for 13,017 earthquakes. *Physics
353 of the Earth and Planetary Interiors*, 200-201:1–9, 6 2012. doi: 10.1016/j.pepi.2012.04.002.
- 354 Faber, K. and Maxwell, P. Geophone spurious frequency: What is it and how does it affect seismic data quality? *Canadian Journal of
355 Exploration Geophysics*, 3:46–54, 1997.
- 356 Fuławka, K., Mertuszka, P., Szumny, M., Stolecki, L., and Szczerbiński, K. Application of MEMS-Based Accelerometers for Near-Field Moni-
357 toring of Blasting-Induced Seismicity. *Minerals*, 12:533, 4 2022. doi: 10.3390/min12050533.
- 358 Gerstoft, P., Fehler, M. C., and Sabra, K. G. When Katrina hit California. *Geophysical Research Letters*, 33, 9 2006. doi: 10.1029/2006GL027270.
- 359 Halford, D. A general mechanical model for $|f|$ spectral density random noise with special reference to flicker noise $1/|f|$. *Proceedings of the
360 IEEE*, 56:251–258, 1968. doi: 10.1109/PROC.1968.6269.
- 361 Harmon, N. and Rychert, C. A. Joint inversion of teleseismic and ambient noise Rayleigh waves for phase velocity maps, an application to
362 Iceland. *Journal of Geophysical Research: Solid Earth*, 121:5966–5987, 8 2016. doi: 10.1002/2016JB012934.
- 363 Harmon, N., Gerstoft, P., Rychert, C. A., Abers, G. A., de la Cruz, M. S., and Fischer, K. M. Phase velocities from seismic noise using beam-
364 forming and cross correlation in Costa Rica and Nicaragua. *Geophysical Research Letters*, 35, 10 2008. doi: 10.1029/2008GL035387.
- 365 Havskov, J. and Alguacil, G. *Seismic Sensors*, pages 13–100. Springer International Publishing, 2016. doi: 10.1007/978-3-319-21314-9_2.
- 366 Herrmann, P., Laroche, S., Wang, H., and Tellier, N. Land Acquisition without Data Jitter Made Possible with MEMS Sensors. *82nd EAGE
367 Annual Conference Exhibition*, pages 1–5, 2021. doi: 10.3997/2214-4609.202112510.
- 368 Herrmann, R. B. Computer Programs in Seismology: An Evolving Tool for Instruction and Research. *Seismological Research Letters*, 84:
369 1081–1088, 11 2013. doi: 10.1785/0220110096.
- 370 Kobayashi, N. and Nishida, K. Continuous excitation of planetary free oscillations by atmospheric disturbances. *Nature*, 395:357–360, 9
371 1998. doi: 10.1038/26427.
- 372 Koymans, M. R., Ballesta, J. D., Ruigrok, E., Sleeman, R., Trani, L., and Evers, L. G. Performance Assessment of Geophysical Instrumentation
373 Through the Automated Analysis of Power Spectral Density Estimates. *Earth and Space Science*, 8, 9 2021. doi: 10.1029/2021EA001675.
- 374 Laine, J. and Mougenot, D. Benefits of MEMS Based Seismic Accelerometers for Oil Exploration. *TRANSDUCERS 2007 - 2007 International
375 Solid-State Sensors, Actuators and Microsystems Conference*, pages 1473–1477, 2007. doi: 10.1109/SENSOR.2007.4300423.
- 376 Laine, J. and Mougenot, D. A high-sensitivity MEMS-based accelerometer. *The Leading Edge*, 33:1234–1242, 11 2014.
377 doi: 10.1190/tle33111234.1.
- 378 Ligorría, J. P. and Ammon, C. J. Iterative deconvolution and receiver-function estimation. *Bulletin of the Seismological Society of America*,
379 89:1395–1400, 10 1999. doi: 10.1785/BSSA0890051395.
- 380 Liu, H.-F., Luo, Z.-C., Hu, Z.-K., Yang, S.-Q., Tu, L.-C., Zhou, Z.-B., and Kraft, M. A review of high-performance MEMS sensors for resource
381 exploration and geophysical applications. *Petroleum Science*, 19:2631–2648, 12 2022. doi: 10.1016/j.petsci.2022.06.005.
- 382 Lognonné, P., Banerdt, W. B., Pike, W. T., Giardini, D., Christensen, U., Garcia, R. F., Kawamura, T., Kedar, S., Knapmeyer-Endrun, B., Margerin,
383 L., Nimmo, F., Panning, M., Tauzin, B., Scholz, J.-R., Antonangeli, D., Barkaoui, S., Beucler, E., Bissig, F., Brinkman, N., Calvet, M., Ceylan,
384 S., Charalambous, C., Davis, P., van Driel, M., Drilleau, M., Fayon, L., Joshi, R., Kenda, B., Khan, A., Knapmeyer, M., Lekic, V., McClean,
385 J., Mimoun, D., Murdoch, N., Pan, L., Perrin, C., Pinot, B., Pou, L., Menina, S., Rodriguez, S., Schmelzbach, C., Schmerr, N., Sollberger,
386 D., Spiga, A., Stähler, S., Stott, A., Stutzmann, E., Tharimena, S., Widmer-Schnidrig, R., Andersson, F., Ansan, V., Beghein, C., Böse, M.,
387 Bozdag, E., Clinton, J., Daubar, I., Delage, P., Fuji, N., Golombek, M., Grott, M., Horleston, A., Hurst, K., Irving, J., Jacob, A., Knollenberg, J.,

- 388 Krasner, S., Krause, C., Lorenz, R., Michaut, C., Myhill, R., Nissen-Meyer, T., ten Pierick, J., Plesa, A.-C., Quantin-Nataf, C., Robertsson, J.,
389 Rochas, L., Schimmel, M., Smrekar, S., Spohn, T., Teanby, N., Tromp, J., Vallade, J., Verdier, N., Vrettos, C., Weber, R., Banfield, D., Barrett,
390 E., Bierwirth, M., Calcutt, S., Compaire, N., Johnson, C., Mance, D., Euchner, F., Kerjean, L., Mainsant, G., Mocquet, A., Manfredi, J. A. R.,
391 Pont, G., Laudet, P., Nebut, T., de Raucourt, S., Robert, O., Russell, C. T., Sylvestre-Baron, A., Tillier, S., Warren, T., Wieczorek, M., Yana,
392 C., and Zweifel, P. Constraints on the shallow elastic and anelastic structure of Mars from InSight seismic data. *Nature Geoscience*, 13:
393 213–220, 3 2020. doi: 10.1038/s41561-020-0536-y.
- 394 McNamara, D. E. and Buland, R. Ambient Noise Levels in the Continental United States. *Bulletin of the Seismological Society of America*, 94:
395 1517–1527, 8 2004. doi: 10.1785/012003001.
- 396 Ogden, C. S., Bastow, I. D., Gilligan, A., and Rondenay, S. A reappraisal of the H– stacking technique: implications for global crustal structure.
397 *Geophysical Journal International*, 219:1491–1513, 12 2019. doi: 10.1093/gji/ggz364.
- 398 Peterson, J. Observations and modeling of seismic background noise, 1993.
- 399 Pike, W. T., Delahunty, A. K., Mukherjee, A., Dou, G., Liu, H., Calcutt, S., and Standley, I. M. A self-levelling nano-g silicon seismometer. *IEEE
400 SENSORS 2014 Proceedings*, pages 1599–1602, 11 2014. doi: 10.1109/ICSENS.2014.6985324.
- 401 Sleeman, R., van Wettum, A., and Trampert, J. Three-Channel Correlation Analysis: A New Technique to Measure Instrumental Noise of
402 Digitizers and Seismic Sensors. *Bulletin of the Seismological Society of America*, 96:258–271, 2 2006. doi: 10.1785/0120050032.
- 403 Tarantola, A. and Valette, B. Generalized nonlinear inverse problems solved using the least squares criterion. *Reviews of Geophysics*, 20:
404 219–232, 5 1982. doi: 10.1029/RG020i002p00219.
- 405 Tellier, N. and Herrmann, P. True Vertical and Orthogonal OBN Sensing with 3C MEMS Sensors. pages 1–4. European Association of Geosci-
406 entists Engineers, 2020. doi: 10.3997/2214-4609.202034022.
- 407 Tomlinson, J. P., Denton, P., Maguire, P. K. H., and Booth, D. C. Analysis of the crustal velocity structure of the British Isles using teleseismic
408 receiver functions. *Geophysical Journal International*, 167:223–237, 10 2006. doi: 10.1111/j.1365-246X.2006.03044.x.
- 409 Wang, Y., Lin, F.-C., and Ward, K. M. Ambient noise tomography across the Cascadia subduction zone using dense linear seismic arrays and
410 double beamforming. *Geophysical Journal International*, 217:1668–1680, 6 2019. doi: 10.1093/gji/ggz109.
- 411 Winder, T., Bacon, C. A., Smith, J. D., Hudson, T., Greenfield, T., and White, R. S. QuakeMigrate: a Modular, Open-Source Python Package for
412 Automatic Earthquake Detection and Location. 2019.
- 413 Woodcock, N. and Strachan, R. *Geological History of Britain and Ireland*. Wiley, 5 2012. doi: 10.1002/9781118274064.
- 414 Zhu, L. and Kanamori, H. Moho depth variation in southern California from teleseismic receiver functions. *Journal of Geophysical Research:
415 Solid Earth*, 105:2969–2980, 2 2000. doi: 10.1029/1999JB900322.